Hindawi
Advances in Civil Engineering
Volume 2023, Article ID 5550967, 17 pages
https://doi.org/10.1155/2023/5550967

Research Article

Deformation Control of Subway Tunnels Undercrossing Airport Facilities: A Case Study of the Xinzheng Airport Rail Transit Hub Project

Zhang Liqiang[1,2] **Jinxing Zhao**[3] **and Qi Le**[4]

[1]*School of Water Conservancy and Transportation, Zhengzhou University, Zhengzhou 450001, China*
[2]*Yellow River Laboratory, Zhengzhou University, Zhengzhou 450001, China*
[3]*Shanghai Tunnel Engineering Co. Ltd., Shanghai, China*
[4]*No.3 Coal Mine Hebi Coal Industry Co. Ltd., Henan Energy Group Co. Ltd., Henan, China*

Correspondence should be addressed to Jinxing Zhao; 305572040@qq.com

Received 19 June 2023; Revised 29 August 2023; Accepted 16 September 2023; Published 27 November 2023

Academic Editor: Wenjun Zhu

The rapid expansion of urban areas due to China's booming economy has led to a conflict between people and vehicular traffic. Consequently, rail transit, represented by subways, has become the primary mode of transportation for residents. However, the influence of soil damage on tunnel deformation is often overlooked in research on the safety of soft soil tunneling, leading to discrepancies between the results predicted by models and the actual settlement of tunnels. In this study, soil investigation and mechanical strength testing were carried out to analyze the impact of aircraft takeoff and landing activities on the Xinzheng Airport facilities. Damage variables are introduced into the Drucker–Prager ideal elastic–plastic criterion, and a soft soil tunneling model with soil deformation is established to investigate the spatial and temporal effects of the shield-cutting force, moving aircraft load, and tunnel deformation. Based on the synchronous grouting technique, a mechanical load-bearing system consisting of a concrete runway, solidified grout, and high-strength segments is formed to ensure the safety of flight activities.

1. Introduction

In major Chinese cities, a 3D commuting network consisting of "elevated expressways + ground-level roads + underground rail transit" is being developed. However, when newly constructed subway tunnels are connected to high-speed rail stations or airports, most existing transportation facilities are already being used. Therefore, protecting the safety of ground buildings is a challenge that tunneling must address.

Shield tunneling, as an efficient method for soft soil tunneling, has the advantages of not affecting ground traffic, producing low noise, and being unaffected by weather conditions. However, there are significant differences in the research focuses of different fields regarding soil settlement and the safety of ground facilities during shield tunneling. Wang et al. [1] proposed a mathematical model consisting of soil loss, thrust parameters, and ground settlement based on the deformation characteristics of shield tunnels and analyzed the influence of soil loss on tunnel settlement in the horizontal X and Y directions using the Peck theory. Xing-Fu et al. [2] analyzed the settlement of soft soils using the Boltzmann function based on the Hangzhou Metro Line 1 project. Their results indicated that the attitude of the shield machine has a significant spatiotemporal effect on soil settlement and that the settlement rate is fast in the early stage and gradually stabilizes in the later stage. Taking the Jinan Yellow River Tunnel project as a case example of large-diameter tunnels required for underground transportation, Ge et al. [3] proposed a Peck formula suitable for determining the settlement of the sedimentary sand of the Yellow River by combining numerical experiments with physical modeling; based on the test results and deformation data from monitoring sections crossing the Yellow River, the settlement of the large-section tunnel was found to be essentially consistent with the width of the settlement trough when tunneling with large-diameter shield machines.

Similarly, to analyze the causes of ground settlement, engineers have shifted their research focus to the damage and failure of rock and soil materials. In this regard, Du et al. [4] noted that damage to intact soil is essentially progressive failure resulting from deformation of the material exceeding the limit of its own elastic modulus. Therefore, based on the theory of materials, an empirical equation was proposed to describe the relationship between damage variables and internal stress and strain, and the required parameters of the equation were obtained from the material strength test results. Given the diverse types of underground tunnels, potential hazards caused by groundwater may be treated prior to construction. Accordingly, Liu et al. [5] analyzed the damage and degradation process of granite during drying with the water content as the research parameter and the methods of image processing, strength testing, and ultrasonic detection and obtained the patterns of internal fracture propagation and failure. Their study indicated that the drying test changes the initial stress environment of granite and that the decrease in water content is the main reason for the decrease in the cohesion of the internal residual soil, eventually leading to the disintegration and failure of the material. Liu et al. [6] characterized the collapsible deformation of saturated loess with soil shear tests and established a yield equation with soil damage variables, which can be used to predict the influence of changes in free water content on soil strength. To investigate the relationship between clay deformation and energy evolution, Jiang et al. [7] conducted triaxial shear tests to analyze the influence of loading modes and pressure levels on the damage to clay samples and concluded that clay can store elastic energy well in the elastic stage, but the samples tend to increase rapidly in volume when approaching their strength limit, with the volume of clay after failure more than 1.8 times that at the initial deformation.

To better control ground settlement, researchers have proposed a variety of constitutive equations for soil failure to analyze the relationship between shield tunneling and soil deformation [8]. However, these studies often focus on solid failure under a single factor and rarely analyze the influence of multiple types of external loads on soil integrity, which is one of the sources of discrepancies between theoretical models and actual settlement. Therefore, in the present study, based on the results of the soil investigation of a subway station, a new Drucker–Prager elastoplastic criterion incorporating damage variables is established to investigate changes in the soil's mechanical strength during the damage process and to obtain the internal stress distribution and settlement results of the soil through which the tunnel passes [9, 10]. In addition, the interaction between mechanical parameters and damage/failure is examined in depth, an optimized shield tunneling process and grouting technique are proposed, and the numerical test results are compared with the actual settlement values of the tunnel to verify the rationality of the model in this study.

2. Overview of the Engineering Project

2.1. Introduction of the Xinzheng Airport Subway Station. In 2019, the Henan provincial government announced a rail transit plan connecting the cities of Zhengzhou and Xuchang. According to the announcement, the starting and ending points of the subway line are the Xinzheng International Airport and the Xuchang East High-speed Railway Station, respectively. The Xinzheng Airport Subway Station is located near Terminal T1 of Xinzheng Airport. The construction includes one subway station and two subway tunnels. The completed tunnel has a V-shaped cross-section, with a maximum slope of 28‰, a minimum slope of 2‰, and a maximum burial depth of 31.42 m from the top of the tunnel to the ground.

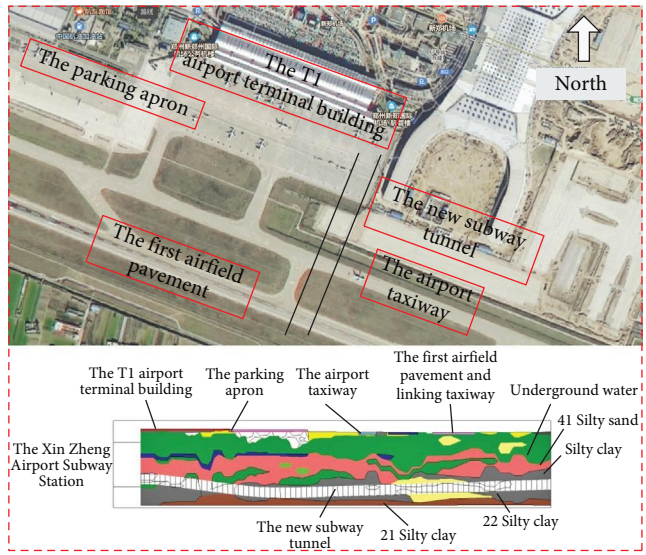

FIGURE 1: Location and crossing soil of Xinzheng Airport Subway Station.

During tunneling, the shield machine passed through different types of soil layers in the following sequence: (1) 22 silty clay, (2) 22G weak calcareous cementation, (3) 22D fine sand, and (4) 41 silty sand. To prevent ground settlement, the tunnel lining was constructed with wedge-shaped rings arranged in a staggered manner. Each segment has an outer diameter of 6.2 m, an inner diameter of 5.5 m, and a ring width of 1.5 m. After segment assembly was completed, the shield machine started multiple rounds of grouting operations to form a load-bearing system consisting of the intact soil layers, solidified grout, and C50 concrete segments to ensure the safety of the tunnel structure. The corresponding plan and section views of Xinzheng Airport and the subway tunnel are shown in Figure 1.

2.2. Main Issues between Shield Tunneling and Ground Settlement. In the study of the settlement patterns of tunnels in soft soil, according to the Peck settlement curve equation, the settlement curve of a single circular tunnel follows a normal distribution, and the ground settlement is closely related to the tunnel area. However, during the construction of a double-line subway tunnel, the total soil settlement is the result of various factors and their combined effects, making it difficult for existing mathematical models to be consistent with the actual engineering results. Especially in the era of mechanized tunneling, the parameters of shield tunneling

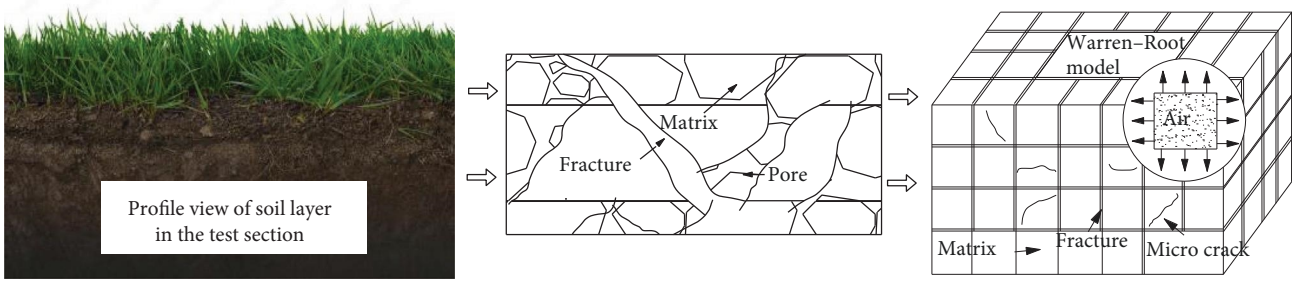

Figure 2: Characteristics of cracks and pores in soil layers.

machines, soil strength, and tunnel support methods have become the key factors determining soil settlement [11, 12].

To ensure personnel safety and tunneling efficiency, a series of measures have been taken to control soil settlement in accordance with the requirements of China's Standard for Design of Shield Tunnel Engineering (2022), for example, selecting higher strength segments, optimizing the tunneling speed, controlling the pressure and quality of synchronous grouting, and performing timely secondary grouting. In contrast, settlement theory and engineering practice still lack a mathematical model that describes the relationship between internal stress changes, meso-microscopic damage to soil, and ground settlement to explain the connection between mesoscopic damage and macroscopic settlement.

3. Mathematical Model for Soil Damage and Ground Settlement under the Influence of Shield Tunneling

3.1. Basic Assumptions of the Mathematical Model. In China, there are various types of tunnels serving different purposes, and their geological conditions vary. Subway tunnels are located mostly in soft soil with an average burial depth of 10–30 m. Under these conditions, the excavated soil is a dual medium filled with fractures and pores, having low strength and integrity [13, 14]. Taking clay as an example, it has an elastic modulus of approximately 0.5–1.4 MPa and a cohesion of only 25–30 kPa. Therefore, to analyze the soil damage process, the mathematical model for the soil layer and the selected elements should satisfy the following assumptions:

(1) The soil layer is a continuum of dual porous media.
(2) The influence of groundwater on the soil strength at the tunnel burial location is ignored.
(3) The variation in tunnel slope is ignored, and the self-weight pressure of the soil layer is considered constant.

3.2. Soil Deformation Equation. As shown in Figure 2, the representative elementary volume (REV) of the simplified soil layer is composed of cracks and pores. Therefore, under internal stress, the deformation equation of the soil can be written in Navier form as follows:

$$Gu_i + \frac{G}{1-2\nu}u_i - \alpha p_f + F_i = 0 \;\; \alpha = 1 - K/K_f \;\; G = \frac{E}{2(1+\nu)}\ , \tag{1}$$

where G, ν, and K are the shear modulus, Poisson's ratio, and bulk modulus of the soil layer, respectively, all of which values can be calculated from the elastic modulus E; F_i is the gravity of the soil layer at the burial depth; similarly, a is the Biot coefficient of the soil, which represents soil compressibility; and P_f is the fluid pressure in the fracture, with the subscript f representing the fracture, and its value is the real-time pressure of the cement grout for this engineering project.

In Equation (1), the first and second terms are the deformation of the REV under in situ stress; the third term is the influence of the grout pressure on the deformation of the REV; and the fourth term is usually replaced by the pressure boundary condition.

3.3. Governing Equation of Cement Grout Flow in Synchronous Grouting. When the footage of the tunnel reaches the preset length, the shield machine stops cutting the soil, and then segment installation and synchronous grouting are carried out. As the cement grout flows out of the grouting holes, the solidified grout causes the segments to consolidate with loose soil layers. Throughout the process, the grout flow rate constantly changes with time; thus, the mass transfer equation can be written as follows [15, 16]:

$$\frac{\partial M_f}{\partial t} + \nabla\left(v_f \cdot \rho_f\right) = Q_s\ , \tag{2}$$

where M_f is the mass of the grout that varies with time and is closely related to the theoretical grouting volume, t is the grouting time, v_f is the grout flow velocity, ρ_f is the grout density, and Qs is the initial grout content in the soil layer, usually 0.

In the mass transport Equation (2), the flow rate of the unsolidified grout can be written as follows:

$$v_f = \frac{k_f}{u_f}\nabla P_f\ , \tag{3}$$

where k_f is the soil fracture permeability, u_f is the dynamic viscosity of the grout, and P_f is the grout pressure.

Equation (2) shows that the grouting pressure is the driving source for the flow of cement grout and that the grouting volume is closely related to the grouting time and the tunnel area. The grouting process is stopped when the design grouting volume is reached, and after the grout solidifies, a new round of tunneling begins.

3.4. Drucker–Prager Ideal Elastic–Plastic Criterion for Soil. In this process, the soil damage variable D is closely related to the tensile and compressive strain in the REV [17, 18], the deformation of which includes both linear elastic deformation and plastic strain increment. Referring to the literature, the tensile and compressive damage variable D [19] of soil REV can be written as follows:

$$D = \begin{cases} 0, \text{Elastic stage} \\ 1 - \left|\dfrac{\varepsilon_{t0}}{\varepsilon_1}\right|^2, \quad \geq \text{Tensile strength} \\ 1 - \left|\dfrac{\varepsilon_{c0}}{\varepsilon_3}\right|^2, \quad \geq \text{Compressive strength} \end{cases}, \tag{4}$$

where ε_{t0} and ε_{c0} are the initial tensile strength and compressive strength of the soil, respectively, which are determined by soil parameters, and ε_1 and ε_3 are the strain in the first and third principal directions of the soil, respectively.

After simplifying the soil layer as an ideal elastic body, the REV inevitably deforms under the shield-cutting force and in situ stress. According to rock damage theory, the degradation of the soil elastic modulus is closely related to the damage state. Based on existing research, the residual elastic modulus of soil, E_d, is related to the damage variable D in the following equation [20, 21]:

$$E_d = E \cdot D. \tag{5}$$

The soil experiences plastic failure when the stress exceeds its strength limit. The Drucker–Prager ideal elastic–plastic criterion [22] can be used to analyze the stress–strain relationship of soil after failure. The constitutive equation can be written as follows:

$$F_D = k_1 I_1' + \sqrt{J_2'} - k_2 - \sigma_p = 0, \tag{6}$$

where k_1 and k_2 are soil mechanical constants, which are determined by the cohesion and plastic dilatancy angle of the soil, respectively, I_1 is the first invariant of the principal stress tensor, J_2 is the second invariant of the effective deviatoric stress tensor, and σ_p is the post-yield stress.

4. Patterns of Soil Damage under the Shield-Cutting Force

4.1. Model Boundary Conditions and Parameter Settings. To analyze the process of shield tunneling and soil deformation in the context of the Xinzheng Airport Station project, based on the mathematical model in Sections 3.2–3.4, the tunnel section in the runway area is selected as the source of the soil damage model for the tunnel undercrossing the airport facilities (airport runway, T1 terminal, and apron).

Referring to the plane strain model in the theory of elasticity, the geometric dimensions of the numerical model are set to 42×43 m (approximately 6.5 times the tunnel diameter). The left and right tunnels are located in the middle of the model and are used to study the influence of secondary stress generated by tunneling on soil damage and ground settlement. The geometric model, boundary conditions, and parameters are shown in Figure 3 and Table 1, respectively.

According to different simulation objects, the geometric model is divided into two parts: soil and tunnel. In terms of the boundary conditions, since the airport facilities are all in use, the upper part of the model is set as the pressure boundary, and the pressure value is closely related to the stress state of the runway. The bottom of the model is a fixed boundary, and the left and right sides are roller support boundaries, which allow only vertical movement.

In Table 1, the different types of parameters can be divided into three categories: soil mechanical strength, cement grout, and synchronous grouting parameters. The values of soil strength parameters are obtained from mechanical experiments conducted during the investigation stage. However, there are no unified approaches among researchers for determining the parameters of synchronous grouting and cement grout. First, the sources of the selected cement grout products are not consistent, leading to variations in the dynamic viscosity of the grout. Second, for the synchronous grouting process, the grouting pressure is closely related to the geological conditions of the driving face, which poses the largest difference between the numerical models and the actual soil layers. Therefore, the values of the above model parameters in this study are obtained from manufacturers' experiments, and their physical definitions are not further elaborated. In Table 2, the physical meaning of boundary conditions is illustrated in Figure 3(b).

To obtain the tunnel deformation and soil stress, clockwise and radial cutting forces are applied at the tunnel boundary to simulate the cutting process of the cutterhead. When the tunnel section is formed, the mesh elements in this area are removed and their mechanical properties are set to zero, and the tunnel boundary is restored to a state of free deformation. The simulation steps show that the calculation of soil displacement requires continuous reference to the results of the previous step. Therefore, the entire numerical experiment must be carried out iteratively. Finally, a monitoring line is selected along the horizontal center of the tunnel to obtain postprocessing data for stress and displacement to evaluate the safety of the tunnel.

4.2. Numerical Model Results

4.2.1. Tunnel Deformation and Ground Settlement under Shield Tunneling. For convenience of analysis, the soil displacement and weight results of the left and right tunnel lines at the time of tunnel formation are extracted for analysis. Their variation patterns are shown below.

Figure 4 shows the contour maps of the soil displacement and weight distribution. After the breakthrough of the

(a)

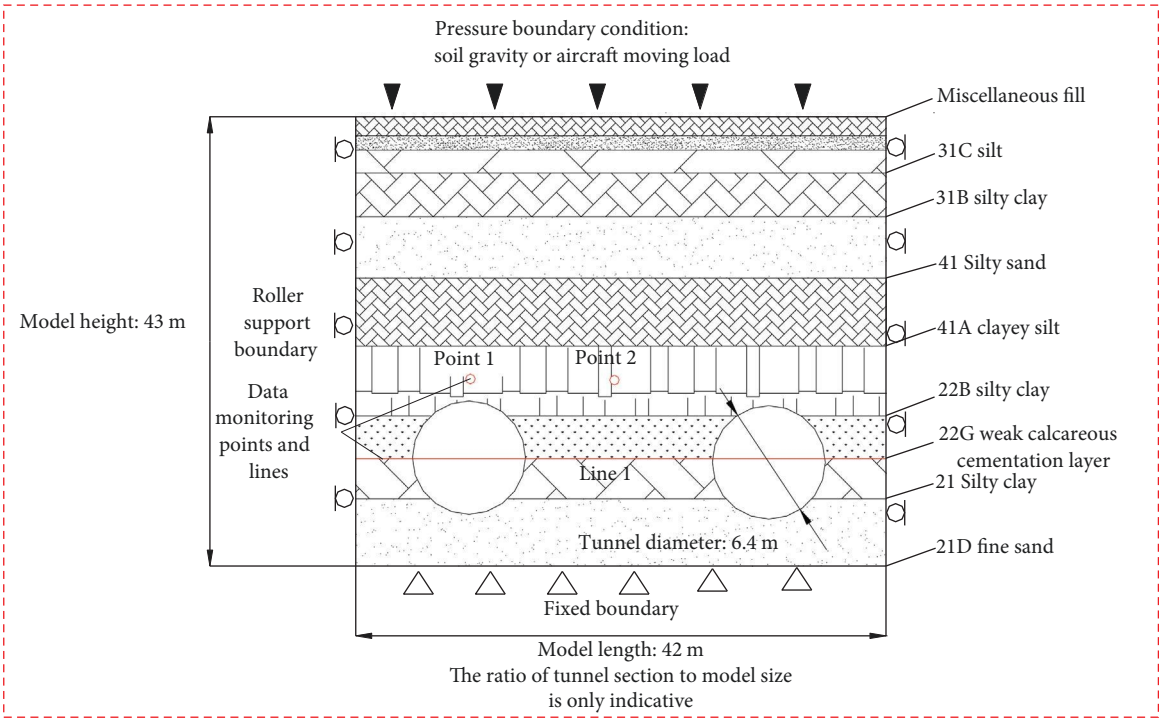

(b)

Figure 3: Geometric modeling of subway tunnels passing through airport facilities: (a) airport flight facilities crossed by subway tunnels; (b) model boundary conditions and parameter setting.

Table 1: Excavation soil layer parameters of Xinzheng Airport Subway Station.

Parameter	Value	Parameter	Value
31C silt elastic modulus E (MPa)	0.15	22B silty clay elastic modulus E (MPa)	0.22
31C silt Poisson's ratio, ν	0.44	22B Poisson's ratio, ν	0.39
31B silt elastic modulus E (MPa)	0.28	21 Silty clay elastic modulus E (MPa)	0.19
31B silt Poisson's ratio, ν	0.42	21 Silty clay Poisson's ratio, ν	0.45
41A silty sand elastic modulus E (MPa)	0.14	Fracture permeability k_f (m^2)	$1.17 \cdot 10^{-12}$
41A silt sand Poisson's ratio, ν	0.44	Synchronous grouting pressure E (MPa)	2
Dynamic viscosity of cement paste μ (Pa s)	$1.84 \cdot 10^{-2}$	Soil tensile strength ε_{t0} (MPa)	0.05
Soil compressive strength ε_{c0} (MPa)	0.1	Cement slurry density	1,300

Table 2: Numerical model boundary conditions.

Boundary condition	Value	Boundary condition	Value
Upper boundary (MPa)	0.8	Initial displacement	0
Lower boundary	Fixed	Left boundary	Roller support
Tunnel boundary	Free deformation	Right boundary	Roller support
Cutting force (MPa)	3	/	

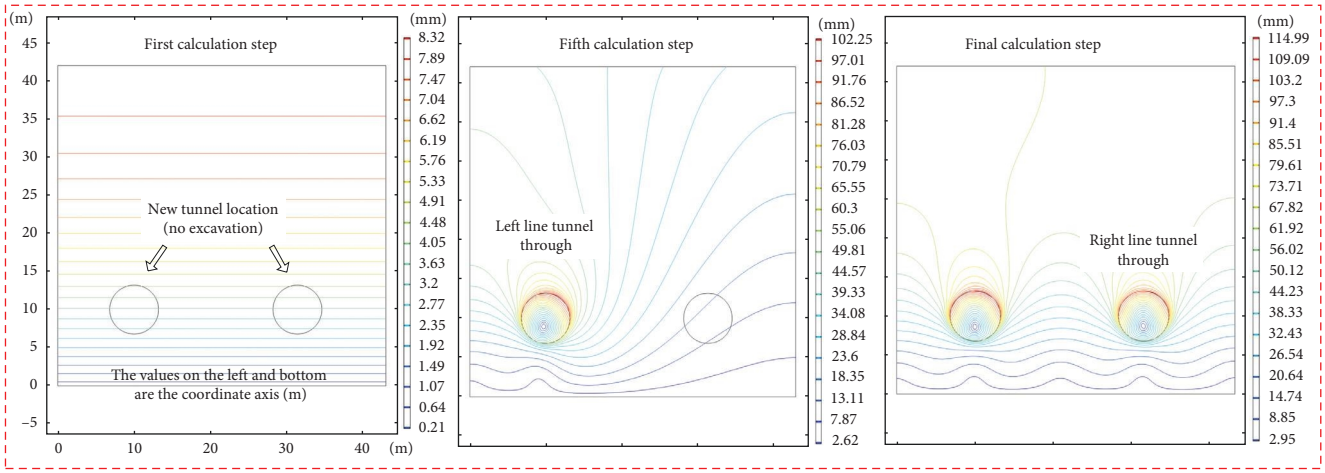

Figure 4: Ground settlement caused by dual-subway tunnel crossing without support: (a) contour map of tunnel displacement under unsupported conditions; (b) distribution of soil layer weight without support (the black element in the figure represents the soil displacement arrow).

tunnel, there are no support measures. Under gravity, the soil above the tunnel continuously invades the tunnel space, which is the fundamental reason for the change in soil displacement. Upon the breakthrough of the left-line tunnel, the shield tunneling under the runway causes a soil settlement of approximately 102 mm, and the maximum settlement occurs directly above the tunnel. With the increase in the number of calculation steps and the breakthrough of the right-line tunnel, the settlement of the later excavated tunnel is significantly higher than that of the first excavated tunnel, the maximum settlement increases to 115 mm, and the overlying soil shows a W-shaped settlement pattern. If no support measures are taken, the large deformation of the soil would lead to the failure of the tunnel crossing.

4.2.2. Internal Stress and Damage Patterns of the Soil under Shield Tunneling. To further illustrate the influence of shield tunneling on soil integrity, the soil around the tunnel is selected as the research object to investigate the extent of damage and the distribution of stress around the tunnel, as shown in Figure 5.

The stress contour maps in Figure 5(a) show that the distribution of stress in the soil is closely related to the number of tunnels and the sequence of tunnel breakthrough.

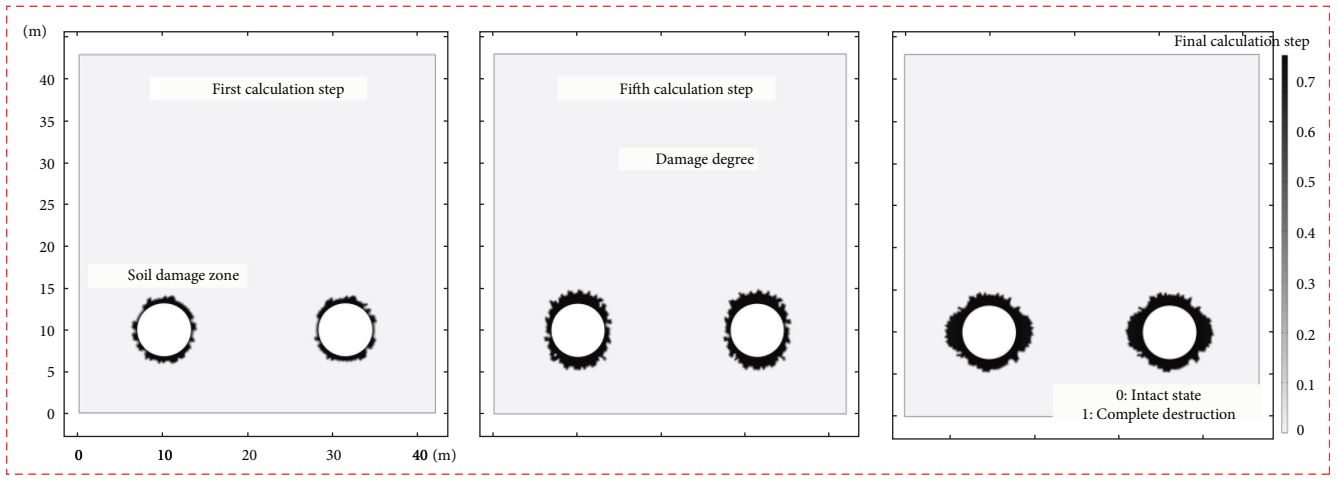

(a)

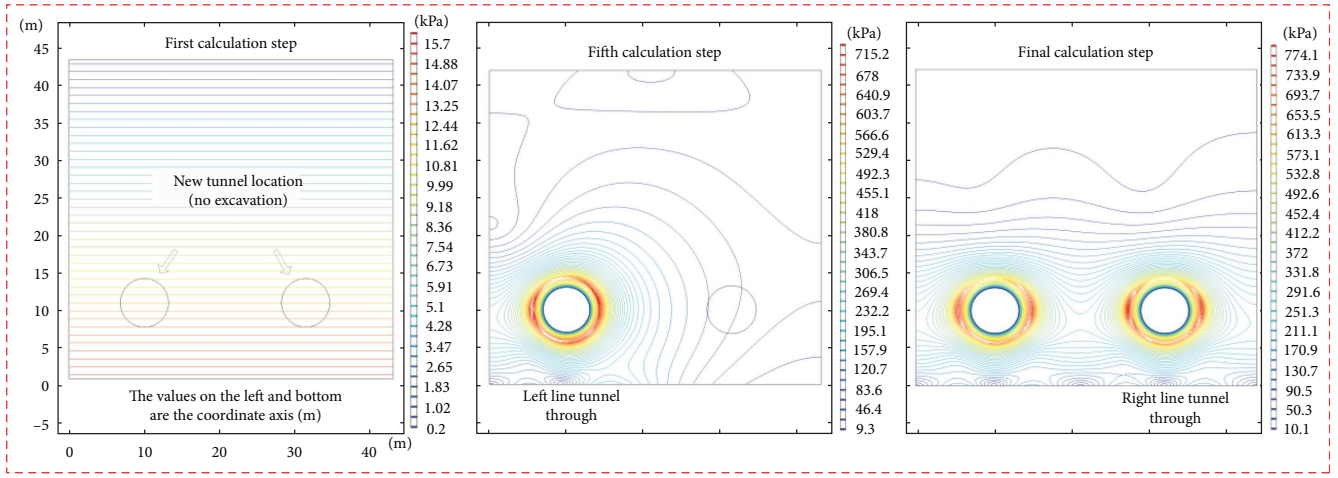

(b)

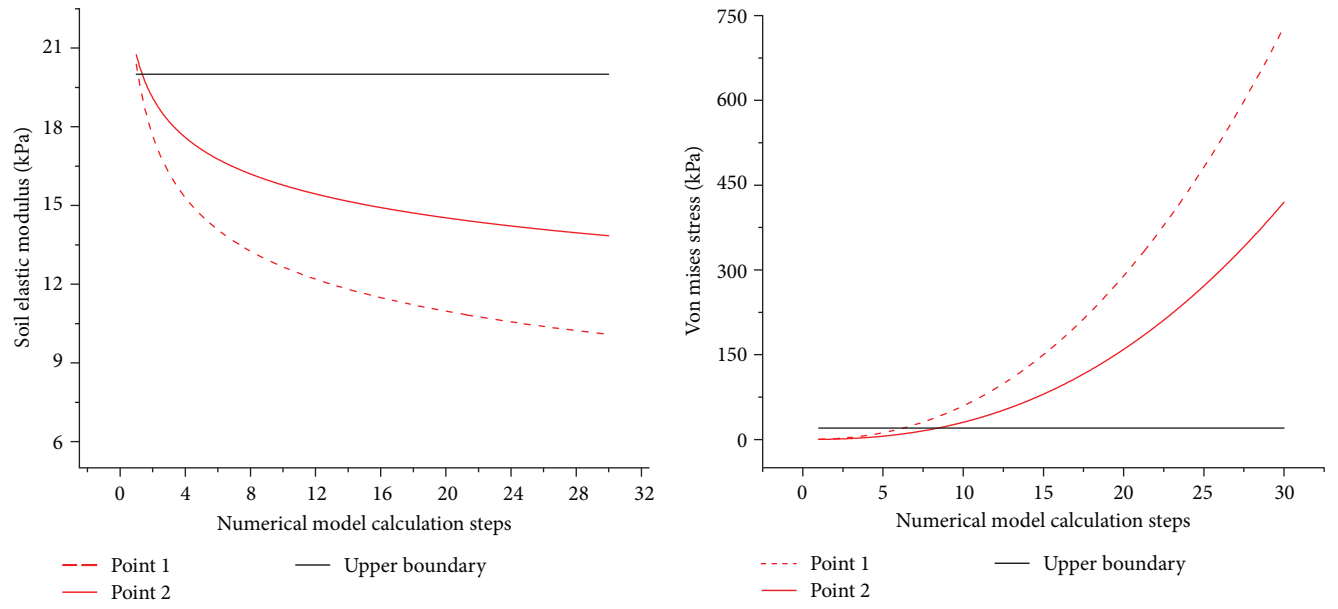

(c)

Figure 5: Soil damage range around the tunnel in different calculation steps: (a) the process of soil damage during subway tunnel excavation; (b) contour map of stress in the soil layer when the subway tunnel runs through; (c) soil strength and internal stress distribution in the damaged area.

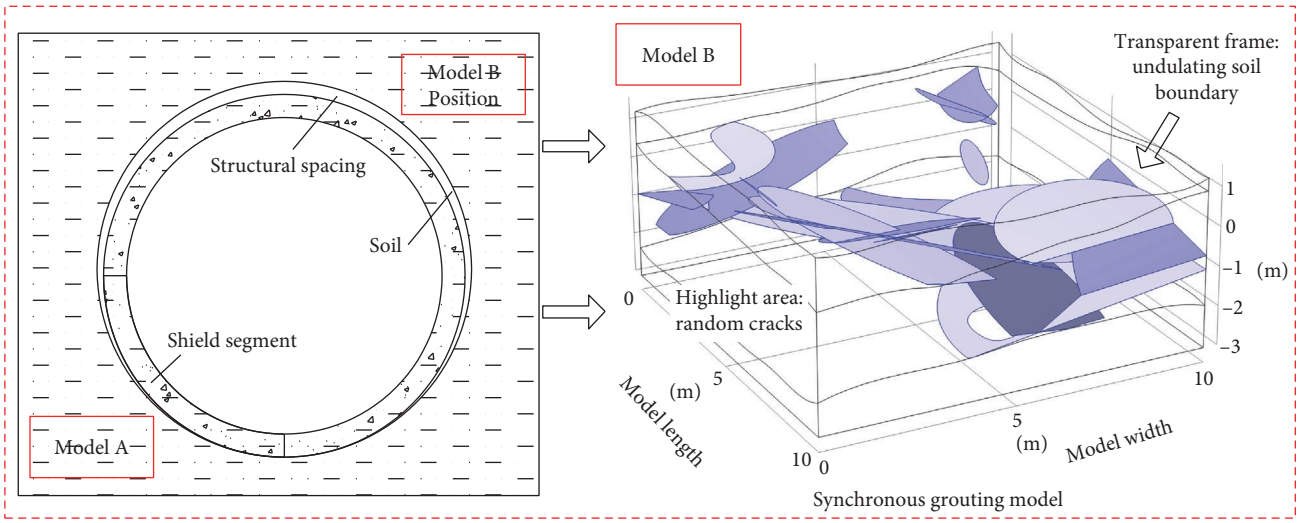

Figure 6: The slurry flow values are divided into parts A and B. The slurry flow model B is taken from the surrounding soil of the tunnel and is divided into two areas from top to bottom building air raid (not shown, replaced by high permeability coefficient) and excavation of the soil layer. According to the level of permeability, the order is building voids > high-permeability soil with cracks (highlighted areas in B are cracks) > remaining soil with fewer cracks.

Table 3: Numerical model boundary conditions.

Boundary condition	Value	Boundary condition	Value
Upper boundary (MPa)	2	Initial displacement	0
Lower boundary	Fixed	Fracture permeability k_f (m^2)	$1.17 \cdot 10^{-12}$
Left boundary Right boundary	No flux	Fracture permeability (solidification) k_f (m^2)	$0.17 \cdot 10^{-17}$

When the left-line tunnel completes the excavation, the initial in situ stress distribution is disrupted, and the stress in the soil around the tunnel increases rapidly to 710 kPa, which considerably exceeds the soil strength limit (25–30 kPa). In comparison, for the right-line tunnel, the secondary disturbance of the soil leads to a further increase in the peak in situ stress. At this stage, the stress in the soil has reached 790 kPa, indicating that the tunnel excavation sequence affects the spatial and temporal distribution of stress in the soil.

Figure 5(b) shows that the extent of damage to the soil around the tunnel expands over time. At this stage, soil failure is influenced by two dominant factors. First, the von Mises stress of the soil is further changed under the combined action of the cutting force of the cutterhead and soil gravity, the interaction of which is the dominant factor for expanding the extent of damage to the soil. Second, the excavation of the tunnel disrupts soil integrity, and the expanded extent of damage causes a rapid decrease in the mechanical properties of the soil, eventually leading to the loss of the soil's bearing capacity and the occurrence of tunnel collapse accidents. By the end of the calculation steps, the extent of damage for the right tunnel expands to approximately 18% of the tunnel radius, indicating that the destruction of soil integrity is a progressive process.

The soil mechanical strength curve shows that during the tunneling process, soil integrity is disrupted, which leads to a decrease in its own elastic modulus. By the end of the calculation steps, the residual elastic modulus of the soil is only 55% of the initial value. The degradation of strength properties intensifies the expansion of damage, resulting in a significantly larger plastic failure zone in the later stage than in the earlier stage. Therefore, it is necessary to carry out support operations in a timely manner.

4.2.3. Characteristics of Grout Distribution and Ground Settlement under Synchronous Grouting. In the tunnel support operations, in addition to the timely installation of reinforced concrete segments, synchronous grouting is used to fill the gaps between the soil and the segments. Therefore, a new cement grout deposition model B is established to analyze the filling effect of the grout in the soil. This model has geometric dimensions of length × width × height = 10 × 10 × 5 m and contains high-permeability fractures with different occurrences. The geometric model is shown in Figure 6.

In the boundary condition settings, the upper part of the model is the grout deposition boundary; that is, the cement grout flows downward sequentially, while the horizontal boundary is a no-flow boundary, which is used to limit the diffusion of grout to the external environment. The parameters required for this model and the soil reinforcement effect are shown in Table 3 and Figure 7, respectively.

According to the governing equation of grout flow in Section 3.3, at the beginning of grouting, the flow of the grout is affected only by the friction of the segment and the

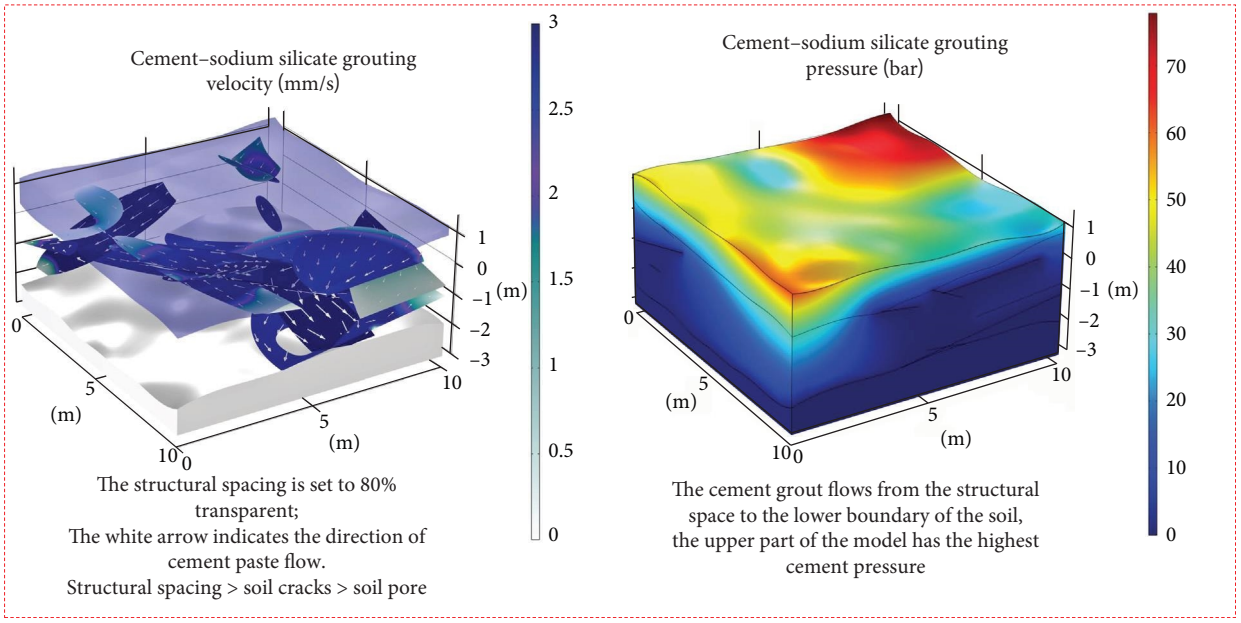

(a)

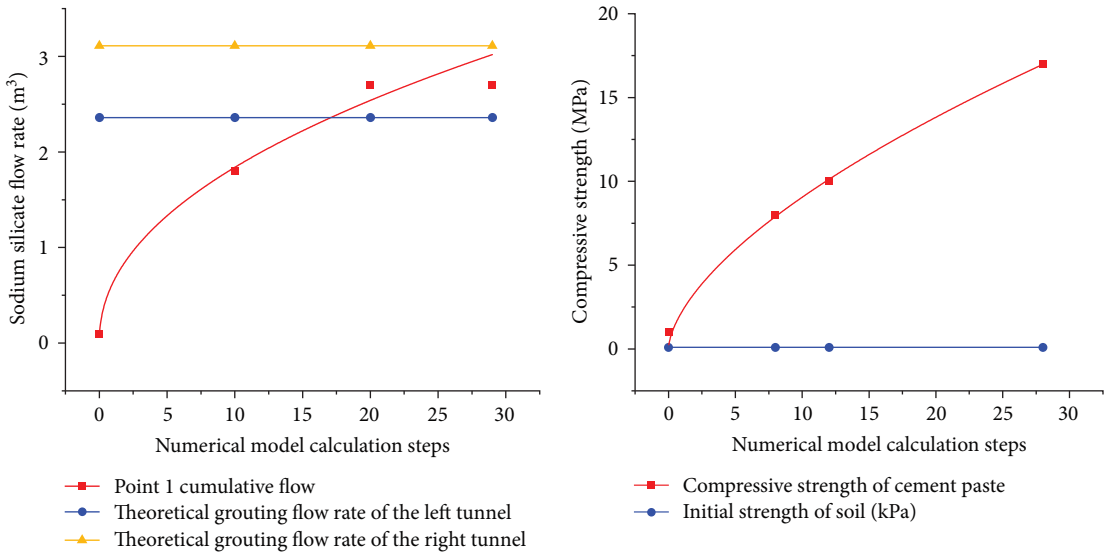

(b)

Figure 7: Continued.

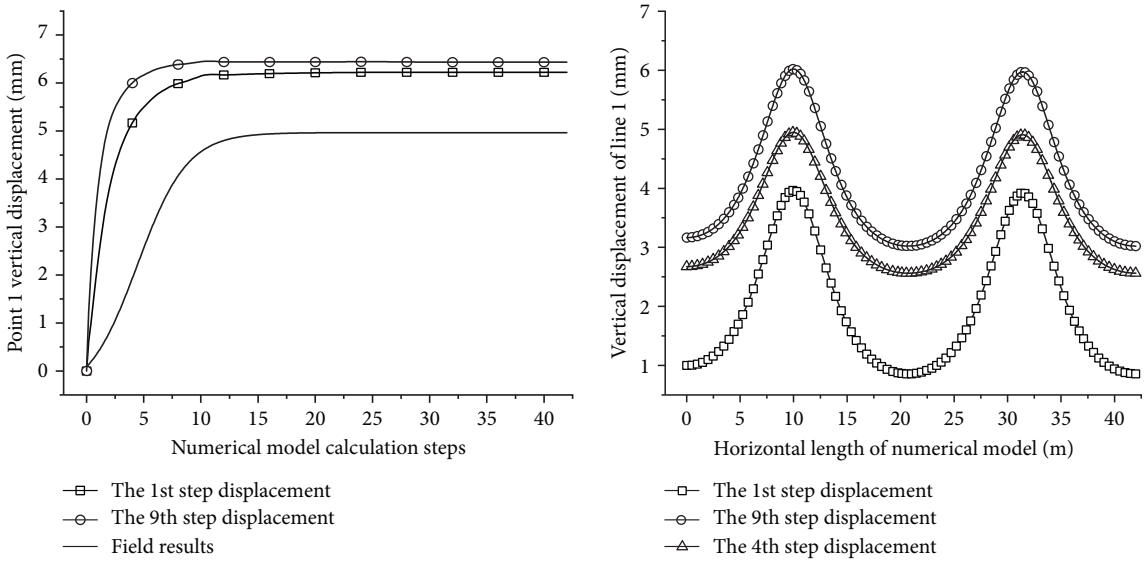

(c)

FIGURE 7: The influence of synchronous grouting activities on the reinforcement effect of soil layers: (a) slurry flow rate and accumulated pressure; (b) changes in synchronous grouting amount and solidification slurry strength over time; (c) settlement deformation value of the tunnel after soil reinforcement.

dynamic viscosity u_f, and the flow resistance of the grout is the smallest at this time. As evident from the contour map of grout distribution in Figure 7(a), the grout outflow moves along the voids of the structure toward high-permeability fractures, and the volume of deposited grout is the result of the combined action of the grouting pressure and its own gravity. In the later stage of synchronous grouting, the fracture space between segments and the soil has been filled with grout, and the solidified grout presents a form of "abundance in the lower part and fullness in the upper part." For the tunnel in this study, the voids of the structure between the rings are 2.36 and 3.11 m^3 ($S_{\text{volume of the cut soil}} - S_{\text{outer volume of the cutterhead in the shield machine}}$), respectively, and the grout growth rate curve in the numerical model is consistent with the filling effect.

The strength curve of the solidified grout shows that with an increase in grouting time, the soil strength in the reinforcement region reaches approximately 18 MPa, which is more than 500 times the initial value, indicating that the solidified grout effectively improves the strength of the loose soil. At this stage, a stable load-bearing system is formed by high-strength segments, solidified grout, and intact soil layers, becoming a key measure to prevent ground settlement. From the results of tunnel settlement during excavation, the cumulative soil settlement is approximately 4–5 mm.

5. Analysis of Tunnel Safety under Aircraft Takeoff and Landing

5.1. Impact of Aircraft Takeoff and Landing on Tunnel Safety. After the completion of the subway tunnel project, airport facilities must serve different types of aircraft, making the long-term safety of the tunnel crucial to the airport operations. During takeoff and landing, the aircraft forms a mechanical transfer system of the runway, soil layers, and tunnel segments through wheels. In this situation, the moving load of the aircraft is the dominant factor causing runway settlement and tunnel deformation.

According to the information provided by the Xinzheng Airport Group, the largest aircraft capable of taking off and landing on the first runway is the A380 passenger aircraft manufactured by Airbus, with a maximum taxiing weight of 562–575 tons and a maximum capacity of 893 passengers. The shape and the landing gear arrangement of the aircraft are shown in Figure 8.

Although modern aircraft landing gears have good cushioning devices, they cannot completely avoid severe impacts on the runway. When an aircraft is taxiing, the front and rear wheels detach from the runway in turn, causing the aircraft's moving load to vary with its position. Therefore, the forces of the landing gears on the runway must be subdivided.

5.2. Tunnel Safety Assessment Model under a Moving Aircraft Load

5.2.1. A380 Moving Aircraft Load. When the A380 aircraft is stationary, all its front and rear wheels are in contact with the ground. There are a total of 11 pairs of wheels, with a longitudinal span of approximately 20 m. The distributed load of each wheel of the aircraft is as follows:

Front-wheel load:

$$F_{\text{nosewheel}} = m_{A380} \cdot \frac{\left(1 - \beta_{\text{landing coefficient}}\right)}{N_{\text{number of front wheels}}} = 5,620 \times \frac{(1 - 0.97)}{2} = 84.3(\text{kN}). \quad (7)$$

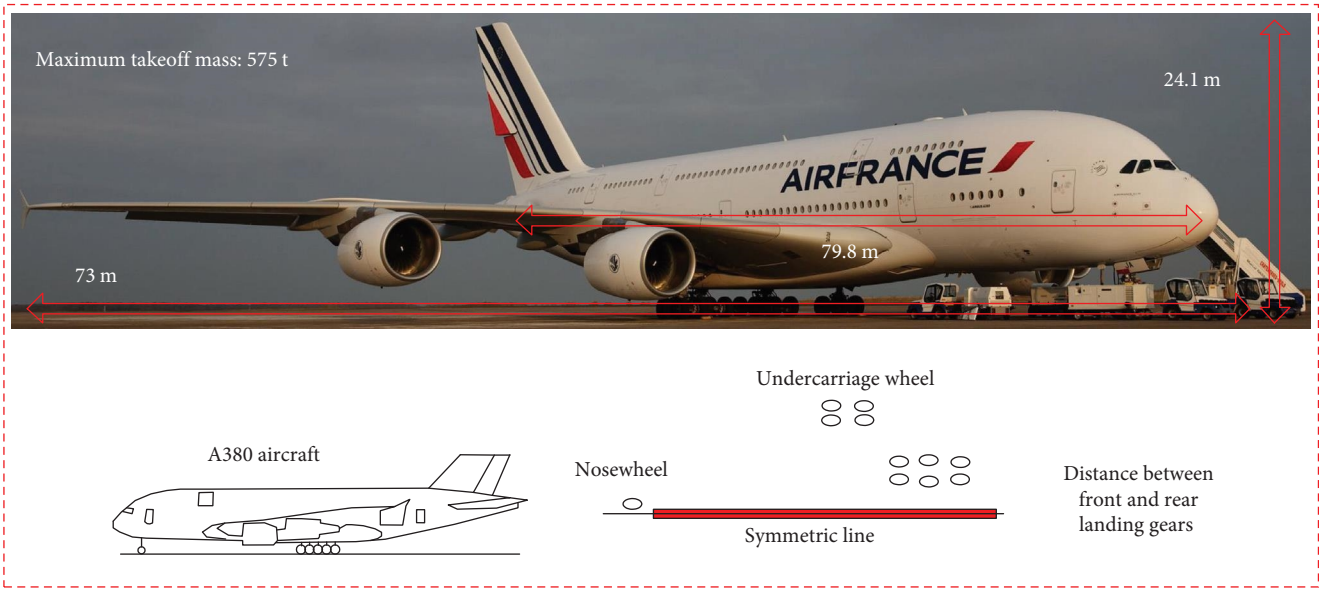

Figure 8: Wheel layout and location of the A380 aircraft.

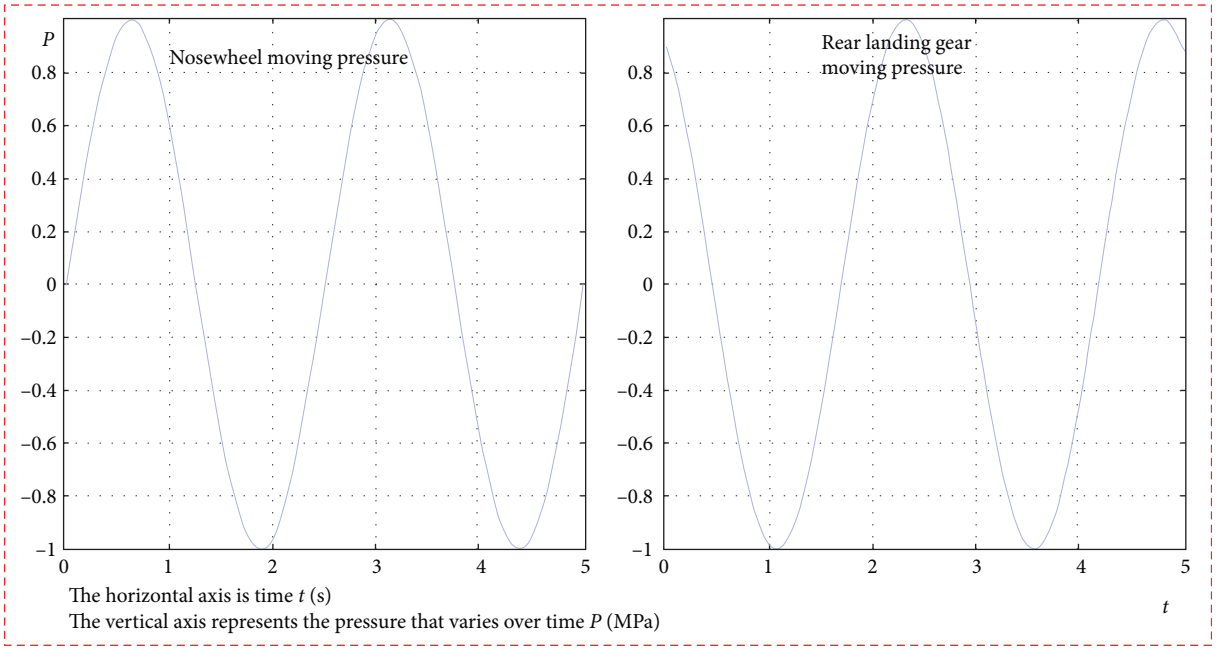

Figure 9: Pressure of the A380 takeoff move load on the runway.

Main landing gear load of the aircraft:

$$F_{\text{land gears}} = m_{\text{A380}} \cdot \frac{\left(1 - \beta_{\text{landing coefficient}}\right)}{N_{\text{number of land gears}}} = 5,620 \times \frac{(1 - 0.97)}{20} = 272.6(\text{kN}) . \quad (8)$$

When the aircraft reaches the takeoff speed, the smoothness of the pavement can deteriorate the stress condition of the runway. The additional impact caused by the aircraft bouncing should also be considered. The rotation frequency of the 1.5-m diameter wheel is as follows:

$$f = 11.8(\text{Hz}) , \quad (9)$$

$$\omega = 2f \cdot \pi = 74(\text{rad/s}) . \quad (10)$$

Thus, the actual moving load of the front wheels on the runway is as follows:

$$F_{\text{moving load of nosewheel}} = F_{\text{nosewheel}} + F_{\text{nosewheel}} \cdot \sin(\omega \cdot t) = 84.3 + 8.43 \sin(74 \cdot t)(\text{kN}) . \quad (11)$$

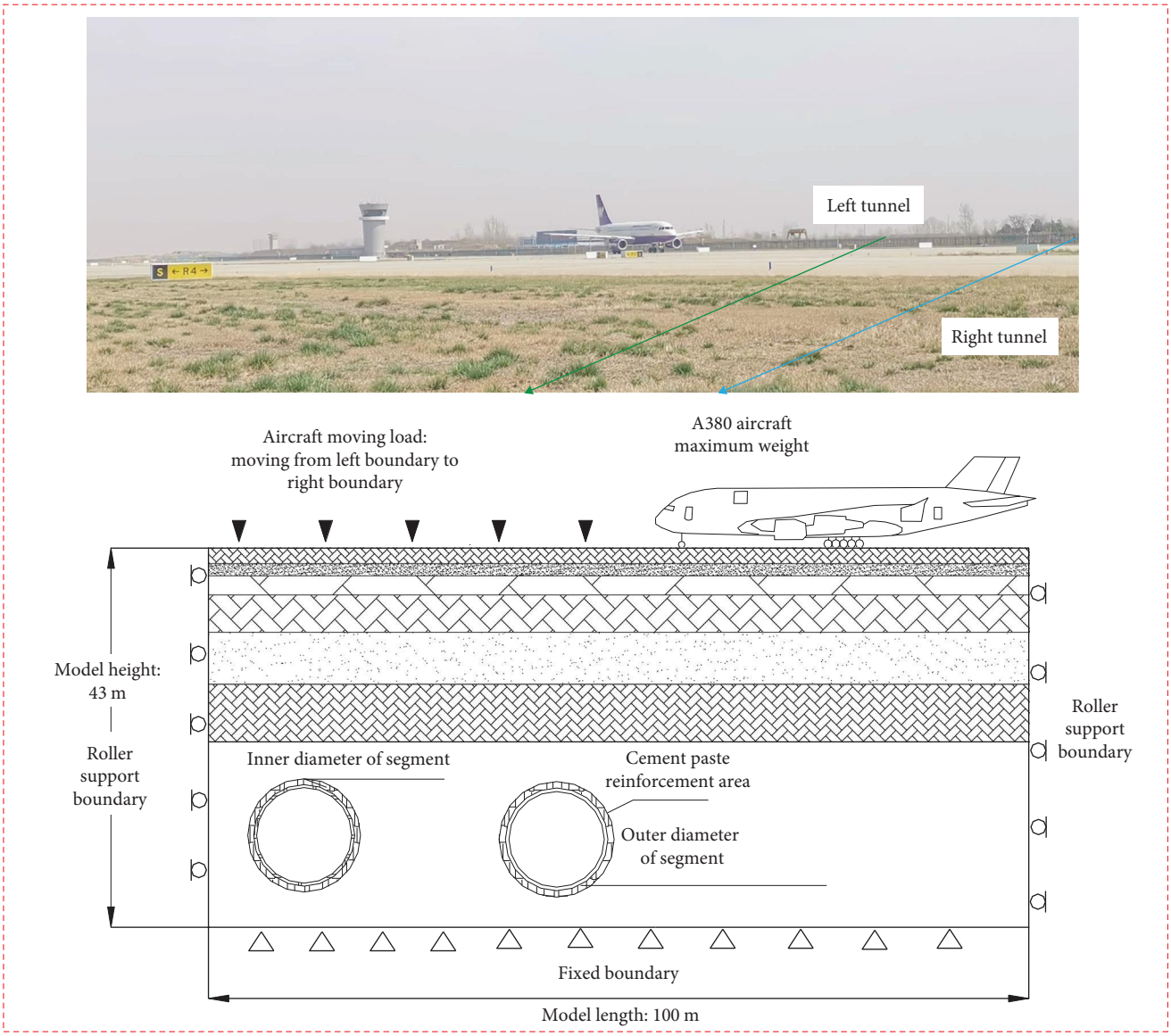

Figure 10: Geometric model of moving load action of A380 aircraft.

Table 4: Subway tunnel segment parameters.

Name	Elastic modulus (Pa)	Poisson's ratio	Cohesion (kPa)	Internalfriction angle (°)
Soil	0.15×10^6	0.4	0.12×10^5	27
Grouting reinforcement ring	18×10^7	0.23	1.5×10^6	35
Lining layer	30×10^9	0.24	/	
Runway	50×10^9	0.15		

The moving load of the rear landing gear is calculated as follows:

$$F_{\text{moving load of landing gears}} = F_{\text{landinggears}} + F_{\text{landinggears}} \cdot \sin(\omega \cdot t) = 272.6 + 27.26\sin(74 \cdot t)(\text{kN}). \quad (12)$$

The moving aircraft load Equations (10) and (12) show that the pressure on the first runway is closely related to time as the aircraft state changes. Therefore, in the COMSOL Multiphysics software, the pressure boundaries of the front and rear wheels are set to be sine and cosine functions, respectively (Figure 9).

5.2.2. Setting the Boundary Conditions of the Numerical Model. In this model, the boundary conditions are divided into two categories: the initial in situ stress zone and the soil reinforcement region (shield segments + solidified grout

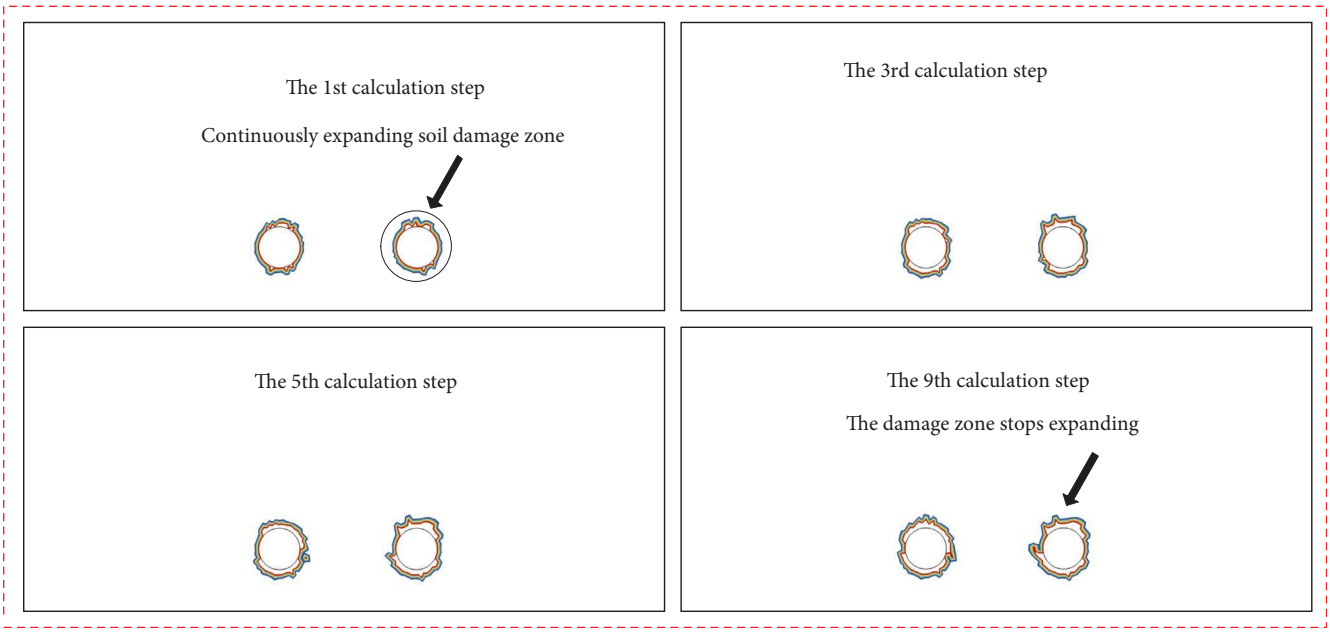

Figure 11: Damage range of the soil layer around the tunnel in different calculation steps.

+ intact soil), based on whether they are actively supported. According to the requirements of China's Code for Design of Railway Tunnel (TB10003-2016), the reinforced concrete segments used in the tunnel assembly are C50 concrete, with an impermeability grade of P12. Furthermore, based on the effect of grout filling in Section 4.2.3, the application of the synchronous grouting process changes the numerical model parameters greatly. At this point, the mechanical parameters of the soil reinforcement region, such as grout strength, are closely related to the solidification time and grout volume. The tunnel safety assessment model under moving aircraft loads is shown in Figure 10.

As shown in the geometric model, to reproduce the influence of the moving aircraft load on the stress and displacement of the soil in different zones, only the aircraft passing along the upper boundary of the model is considered; there is no takeoff effect, and the pressure distribution varies with the aircraft position. Accordingly, the upper boundary is set to be the moving aircraft load that varies with position, and the other boundary conditions remain the same as before.

The synchronous grouting greatly enhances the mechanical properties of the initial soil, leading to significant differences in the parameter results compared to those in Section 4.1. Accordingly, the parameters of the new model are obtained according to the relevant literature and segment strength data, as shown in Table 4.

5.2.3. Influence of Moving Aircraft Load on Soil Stress. To explore the influence of the moving aircraft load on the deformation of the runway, soil, and tunnel support structure, the analysis focuses on the moving aircraft load and the soil stress. The change process is as follows.

As shown by the von Mises stress in the soil, the soil's upper boundary is in direct contact with the moving aircraft load, causing the peak internal stress to increase rapidly to 15 MPa. As the aircraft load moves toward the right side of the model, this process results in a constantly changing state of the peak and zone of stress in the soil. Comparison with the stress of the completed tunnel reveals that the soil layer in the grouting reinforcement region and the assembled high-strength segments are the main components carrying the moving load. Despite a peak internal stress as high as 25 MPa, the distribution of internal stress caused by the moving aircraft load is completely different from the results in Section 4.

The peak and zone of stress in the soil are much smaller in the case of tunnel excavation than in the case of moving aircraft load, which is the fundamental reason why the extent of damage to the soil around the tunnel is smaller than the latter. Second, after the completion of the tunnel, the elastic modulus of the soil has already been in a damaged state compared to the initial soil environment (see Figure 5). Although measures such as synchronous grouting have improved the soil strength in the later stage, the takeoff and landing of aircraft increase the moving load carried by the tunnel more than 20-fold, once again destructing the integrity of the residual soil. This phenomenon is the source of long-term settlement of the soil and the tunnel.

5.2.4. Influence of the Moving Aircraft Load on the Extent of Damage to the Soil in the Reinforcement Region. To further analyze the influence of the moving aircraft load on soil damage in the reinforcement region, the extent of soil damage in this region is selected as the research object. The propagation process with different calculation steps is shown in Figure 11.

In all calculation steps, the moving aircraft load first acts on the left side of the model and then transfers to the soil layer on the right side. At this time, the extent of damage for the left-line tunnel is approximately 0.07 times its own diameter.

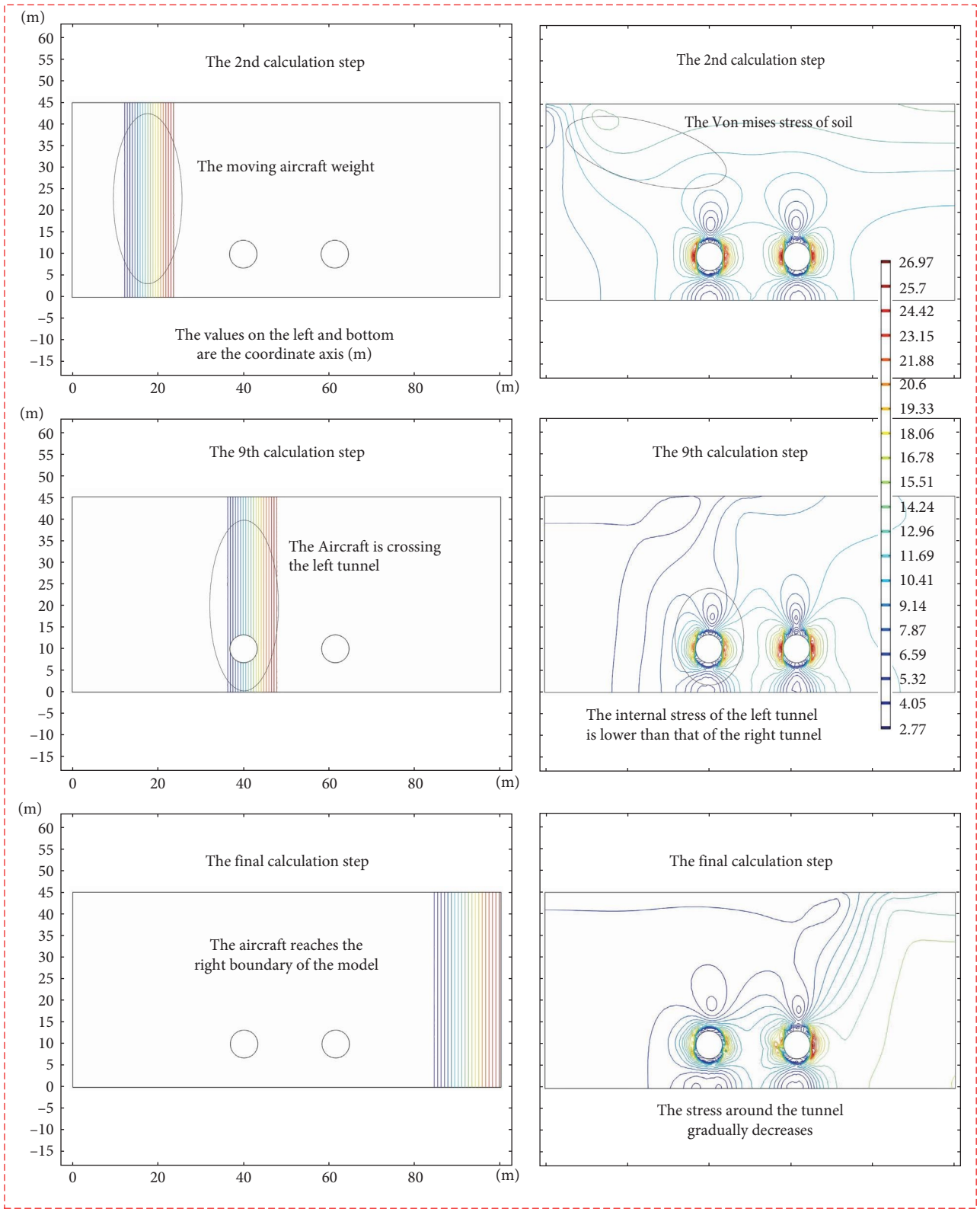

Figure 12: Change process of the moving aircraft load across the tunnel.

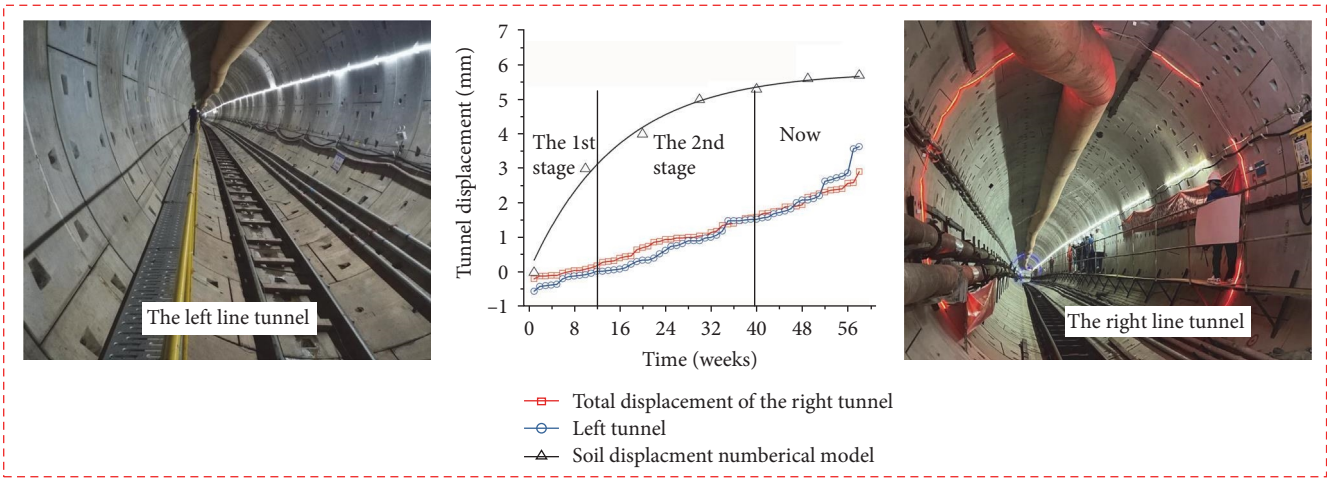

(a)

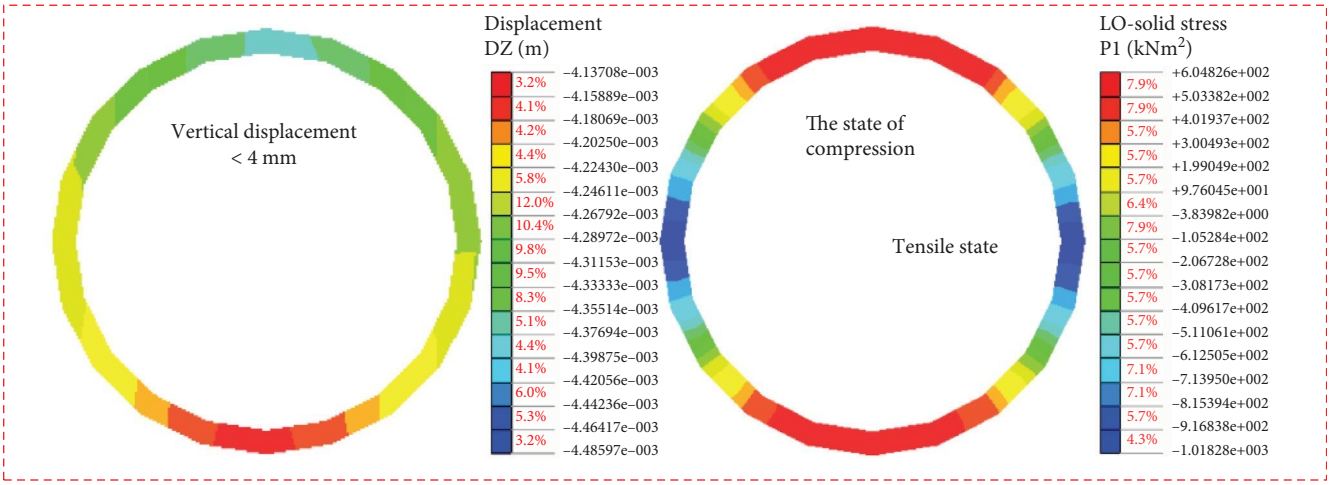

(b)

Figure 13: Soil settlement curve in different regions: (a) influence of aircraft moving load on soil settlement; (b) influence of the aircraft moving load on segment displacement.

In comparison, the extent of damage for the right-line tunnel is only 0.03–0.04 times. The temporal difference is the direct cause of the asynchronous expansion of the extent of damage between the two. When the aircraft moves above the two tunnels, they carry the moving load simultaneously, which leads to the fastest growth of the extent of soil damage, with a maximum zone of approximately 0.095–0.097 times the tunnel diameter. As the aircraft gradually moves away from the existing tunnels, the soil damage stops, with its maximum boundary being approximately 0.112 times its diameter.

A summary of the expansion process of soil damage shows that the internal stress change caused by the moving aircraft load is the dominant factor in soil failure around the tunnel, and the extent of damage varies with the aircraft's position. Therefore, stresses in different zones of the model are ranked in ascending order as the initial in situ stress zone < the aircraft dynamic load influence zone < the stress concentration zone around the tunnel (as confirmed by the results in Figure 12).

5.2.5. Influence of Moving Aircraft Load on the Deformation of the Concrete Runway and High-Strength Segments. In the safety assessment of tunnels regarding moving aircraft loads, segment deformation and especially runway settlement are the core research focus. In this case, the deformation of the first runway and the concrete segments is shown in Figure 13.

In the first stage, when the aircraft moves toward the left side of the model, the soil settlement has occurred in this area, with a displacement of approximately 1.5–2.2 mm (Figure 13(a)). However, When the moving aircraft load acts on the top of the tunnel, the stress in the soil reaches its peak, the runway settlement reaches its maximum, which is approximately 4–5 mm, and the cumulative settlement during this period is slightly higher than that during tunneling but is still within the safe range (the 2nd stage). Finally, as the aircraft leaves the model boundary, the tunnel settlement no longer increases, and the final soil settlement is 5–6 mm.

Compared to the situation of slow in situ stress, the moving aircraft load has a short duration and generates high peak pressure. The load-bearing system formed by high-strength segments and the reinforced soil fully absorbs the impact caused by the taxiing of an aircraft. The evaluation of the strain of segments reveals the segments are still within the elastic limit, and the tunnel deformation is controlled within 0.1%. Therefore, the deformation of the runway and the tunnel is the result of the joint support provided by the load-bearing system.

6. Conclusion

This study examines the safety and settlement control of operating airport facilities during the construction of undercrossing double-line shield tunnels. Based on the principles of soil mechanics and the Peck settlement theory, the influences of double-line tunneling and aircraft taxiing, takeoff, and landing on the extent of soil damage are investigated. The main conclusions are as follows:

(1) On the basis of the ideal elastic–plastic criterion, a mathematical model of soil damage under double-line tunneling is established. The results show that the spatial and temporal sequence of tunneling has a significant impact on the settlement of airport facilities and that the total displacement results from the combined effects of soil damage, support structures, and spatial and temporal changes in internal stress.

(2) Measures such as synchronous grouting and secondary grouting are implemented to eliminate the potential threat to tunnel safety caused by aircraft takeoff and landing. The injection of the flowing grout effectively fills the cracks in the soil and improves the strength of the loose soil. Additionally, the support system formed by the runway concrete layer, solidified grout, and high-strength segments become the main load-bearing system for external loads.

(3) To ensure the long-term safety of tunnels and airport facilities, the control measures of "safety assessment plan before crossing + safety control measures during crossing + settlement monitoring system after crossing" are established. According to the displacement data, the combined application of multiple measures helps transfer the peak stress to the deep part of the soil and contributes to the safe use of the tunnel.

Data Availability

The data used to support the findings of this study are available from the corresponding author upon request.

Conflicts of Interest

The authors declare that they have no conflicts of interest.

Acknowledgments

The authors gratefully acknowledge the support from the Shanghai Super Postdoctoral Program.

References

[1] J. Wang, X. Liu, S. Liu, Y. Zhu, W. Pan, and J. Zhou, "Physical model test of transparent soil on coupling effect of cut-off wall and pumping wells during foundation Pit dewatering," *Acta Geotechnica*, vol. 14, pp. 141–162, 2019.

[2] Y. U. Xing-Fu, Z. Hong-Wu, Z. Li, and L. I. Jun-Wen, "Analysis of the three treatments for failures of a high-steep highway slope," Chinese Journal of Rock Mechanics & Engineering, 2005.

[3] Y. Ge, Y. Liu, P. Lin, and Z. Xu, "Effects of rock properties on the wear of tbm disc cutter: a case study of the yellow river diversion project, china," *International Journal of Geomechanics*, vol. 22, no. 4, Article ID 04022011, 2022.

[4] B. Du, H. Bai, M. Zhai, and S. He, "Experimental study on dynamic compression characteristics of red sandstone under wetting–drying cycles," *Advances in Civil Engineering*, vol. 2020, Article ID 6688202, 10 pages, 2020.

[5] Y. Liu, Y. Zhang, R. Wu, J. Zhou, and Y. Zheng, "Nonexistence and non-decoupling of the dissipative potential for geomaterials," *Geomechanics and Engineering*, vol. 9, no. 5, pp. 569–583, 2015.

[6] W. Liu, Q. Yang, X. Tang, and W. Li, "Experimental study on the dynamic characteristics of silt clay subjected to drying–wetting cycles under cyclic loading," *Journal OF Hydraulic Engineering*, vol. 46, no. 4, pp. 425–432, 2015.

[7] Q. Jiang, J. Cui, and J. Chen, "Time-dependent damage investigation of rock mass in an in situ experimental tunnel," *Materials*, vol. 5, no. 8, pp. 1389–1403, 2012.

[8] H. Jiang, A. Jiang, and M. Xu, "Research on algorithm and coupling damage model of rock under high temperature and loading based on mohr-coulomb criterion," *International Journal of Computational Methods*, vol. 19, no. 4, Article ID 2250001, 2022.

[9] Z. Z. Wang, Y. J. Jiang, and C. A. Zhu, "Seismic energy response and damage evolution of tunnel lining structures," *European Journal of Environmental and Civil Engineering*, vol. 23, no. 6, pp. 758–770, 2019.

[10] X.-Z. Liu, Y.-L. Sang, L.-M. Xin, G. Shi, and J.-X. Wu, "Structural damage of subway tunnel buried shallowly in silt layer under soil mound loading," *Advances in Civil Engineering*, vol. 2020, Article ID 4513761, 11 pages, 2020.

[11] H. Sui, C. Ma, C. Dai, and T. Yang, "Study on stability of shield tunnel excavation face in soil-rock composite stratum," *Mathematical Problems in Engineering*, vol. 2021, Article ID 5579103, 19 pages, 2021.

[12] W. Zhu, C. Yang, Z. Yu, J. Xiao, and Y. Xu, "Impact of defects in steel-concrete interface on the corrosion-induced cracking propagation of the reinforced concrete," *KSCE Journal of Civil Engineering*, vol. 27, no. 6, pp. 2621–2628, 2023.

[13] D. I. Sheng-Jie, W. Ming-Yuan, D. Nan-Sha, and S. Qing-Tao, "Numerical simulation study on Rev's measure of soil–rock mixture," *Journal of Disaster Prevention and Mitigation Engineering*, vol. 32, no. 5, pp. 523–527, 2012.

[14] W. Zhu, Z. Yu, C. Yang, F. Dong, Z. Ren, and K. Zhang, "Spatial distribution of corrosion products influenced by the initial defects and corrosion-induced cracking of the concrete," *Journal of Testing and Evaluation*, vol. 51, no. 4, pp. 2582–2597, 2023.

[15] P. Li, J. Liu, L. Shi, Y. Zhai, D. Huang, and J. Fan, "A semi-elliptical surface compound diffusion model for synchronous grouting filling stage in specially shaped shield tunnelling," *International Journal for Numerical and Analytical Methods in Geomechanics*, vol. 46, no. 2, pp. 272–296, 2022.

[16] Z. Zhou, Z. Liu, B. Zhang, W. Gao, and C. Zhang, "Grouting pressure distribution model for the simultaneous grouting of shield tunneling while considering the diffusion of slurry," in *Advances in Environmental Vibration and Transportation Geodynamics*, E. Tutumluer, X. Chen, and Y. Xiao, Eds., vol. 66 of *Lecture Notes in Civil Engineering*, pp. 793–809, Springer, Singapore, 2020.

[17] P. Li, L. Yan, and D. Yao, "Study of tunnel damage caused by underground mining deformation: calculation, analysis, and reinforcement," *Advances in Civil Engineering*, vol. 2019, Article ID 4865161, 18 pages, 2019.

[18] G. Walton, M. Lato, H. Anschütz, M. A. Perras, and M. S. Diederichs, "Non-invasive detection of fractures, fracture zones, and rock damage in a hard rock excavation—Experience from the Äspö hard rock laboratory in Sweden," *Engineering Geology*, vol. 196, pp. 210–221, 2015.

[19] Q. Y. Wang, W. C. Zhu, T. Xu, L. L. Niu, and J. Wei, "Numerical simulation of rock creep behavior with a damage-based constitutive law," *International Journal of Geomechanics*, vol. 17, no. 1, pp. 4016041–4016044, 2017.

[20] W. Jun-Xiang, J. An-Nan, and S. Zhan-Ping, "Study of the Coupling Model of Rock Elastoplastic Stress-Seepage-Damage (i): Modelling and its Numerical Solution Procedure," Rock and Soil Mechanics.

[21] M. Zhao, Y. Cheng, Z. Song et al., "Stability analysis of TBM tunnel undercrossing existing high-speed railway tunnel: a case study from Yangtaishan tunnel of Shenzhen metro line 6," *Advances in Civil Engineering*, vol. 2021, Article ID 6674862, 18 pages, 2021.

[22] S. Zhang, S. He, J. Qiu, W. Xu, R. S. Garnes, and L. Wang, "Displacement characteristics of an urban tunnel in silty soil by the shallow tunnelling method," *Advances in Civil Engineering*, vol. 2020, Article ID 3975745, 16 pages, 2020.